



## Facile assembled biochar-based nanocomposite with improved graphitization for efficient photocatalytic activity driven by visible light



Shujing Ye<sup>a,b,1</sup>, Min Yan<sup>a,b,1</sup>, Xiaofei Tan<sup>a,b,1</sup>, Jie Liang<sup>a,b,1</sup>, Guangming Zeng<sup>a,b,\*</sup>, Haipeng Wu<sup>a,b,c,\*</sup>, Biao Song<sup>a,b</sup>, Chengyun Zhou<sup>a,b</sup>, Yang Yang<sup>a,b</sup>, Han Wang<sup>a,b</sup>

<sup>a</sup> College of Environmental Science and Engineering, Hunan University, Changsha, 410082, PR China

<sup>b</sup> Key Laboratory of Environmental Biology and Pollution Control (Hunan University), Ministry of Education, Changsha, 410082, PR China

<sup>c</sup> College of Life Sciences, Hebei University, Baoding, 071002, PR China

### ARTICLE INFO

#### Keywords:

Carbon-based nanocomposite  
Visible-light photocatalysis  
Porous graphite biochar  
Graphitization  
g-MoS<sub>2</sub>

### ABSTRACT

The preparation processes of efficient photocatalyst containing defect regulation and heterostructure construction are usually complicated and difficult to control at present, besides, the catalyst agglomeration in solution further limits their application. There is an urgent need for designing a potentially cheap, efficient, sustainable and easy-prepared nanocomposite to improve photocatalytic performance. In present study, the facile synthesized porous graphitic carbon with microtubular structure, high graphitization degree and abundant porosity demonstrates an outstanding advantage of excellent conductivity and facilitated mass transport. Such porous graphite biochar (PGBC) self-assembled with g-MoS<sub>2</sub> nanosheets is observed by the optimized band gap, enhanced visible light harvesting, accelerated charge transfer and efficient photo-generated carrier's separation. Considering the favorable specific surface area and pore distribution of PGBC for avoiding nanosheet agglomeration, the as-prepared composites display quite high efficiency for tetracycline hydrochloride (TC) removal based on the synergistic action of the desirable absorption and photocatalytic capability. Mechanism exploration indicates that surface adsorption is mainly dominated by electrostatic interaction, hydrogen bonding, π-π stacking and pore-filling, and hole (h<sup>+</sup>) and hydroxyl radical (OH) are the predominant active species responsible for TC degradation. Furthermore, the nanocomposites possess advisable stability performance for TC removal in contaminated river water, further providing an underlying insight for establishing high-efficient and easy-prepared photocatalysts in practical contaminated water remediation.

### 1. Introduction

Antibiotic contamination resulted from human abuse of pharmaceuticals has raised world-wide concerns, owing to the indefinite environmental impacts and threats to the organisms in ecosystem [1–4]. Numerous studies were conducted for solving this environmental issue, including biological technology (degrading-organism) [5–7], chemical technology (advanced oxidation, photo-catalysis) [8–10] and physical technology (separation) [11–13]. In recent years, nanostructured porous graphitic carbon (PGC) has drawn huge deal of scientific interests to be used as advanced carbon materials for energy storage [14–16] and environmental remediation [17–19], based on their excellent electrical characteristics and porous structure [20,21]. Unfortunately, the productive processes of PGC with expensive chemical precursors, harmful reagents and catalysts, high energy/time-

consuming steps restrict their large-scale application. Hence, a low-cost, eco-friendly and effective approach for preparing PGC by renewable biomass is highly desirable [22,23], where product is known as porous graphitic biochar (PGBC). Straw is mainly composed of lignin, cellulose and hemicellulose, and it poses plentiful polar hydroxyl and carbonyl groups, which is endowed as precursor of carbon material with excellent properties. Preparing remediation material by straw is beneficial to realize the green disposal by reuse of agricultural waste on the basis of the concept “waste to wealth”.

Photocatalytic degradation of organic pollutants is an economic, green and wide-accepted technology, and the development of photocatalyst is the focus of research [23–27]. Semiconductor materials play an important role in photocatalysis with effective solar energy conversion. Among them, hierarchical graphene-like molybdenum disulfide (g-MoS<sub>2</sub>), a transition metal dichalcogenides, with ultrathin-

\* Corresponding authors at: College of Environmental Science and Engineering, Hunan University, Changsha, 410082, PR China.

E-mail addresses: [zgming@hnu.edu.cn](mailto:zgming@hnu.edu.cn) (G. Zeng), [wuhaipeng0701@126.com](mailto:wuhaipeng0701@126.com) (H. Wu).

<sup>1</sup> These authors contributed equally to this article.

layered structure is found to have an appreciable bandgap of about 1.89 eV in its monolayer regime [28,29]. Although the relatively narrow band is advantageous to the generation of photoexcited electrons, the catalytic effect of pure MoS<sub>2</sub> is not satisfactory because of high recombination of photoexcited carriers. Therefore, the modifications of MoS<sub>2</sub>, such as constructing heterojunction with one or more semiconductors [30–32] and doping with transition metal or nonmetal ions [33], have attracted great attention on field of adsorption, electronics and optoelectronics. For example, an efficient photocatalytic degradation with Z-scheme system of Ag<sub>3</sub>PO<sub>4</sub>/MoS<sub>2</sub> was confirmed by Zhu et al. [34], in which Ag particles formed by in situ reduction from Ag<sup>+</sup> on interfacial surface of Ag<sub>3</sub>PO<sub>4</sub>/MoS<sub>2</sub> could act as the charge separation center for effectively prolonging the lifetime of photo-generated carriers and successfully inhibiting the photocorrosion of Ag<sub>3</sub>PO<sub>4</sub>. However, the complicated preparation process of polynary heterojunctions inevitably affects the wide application of this type of photocatalyst in actual water treatment.

Photon absorption and charge separation efficiency are two major bottlenecks limiting the development of photodegradation [35,36]. PGBC posing high conductivity as well as the favorable functional groups can effectively facilitate the electron transport and enhance the electrochemical utilization, but there are few reports on its application in the field of photocatalysis. PGBC with highly-perfect graphitization and porous structure could be served as a good support for the loading of nanoparticles. Incorporation of PGBC into MoS<sub>2</sub> nanostructure, on one hand, the porous structure with larger accessible surface areas might allow g-MoS<sub>2</sub> nanosheets to be deposited thereby avoids nanoparticle agglomeration. On the other hand, the high graphitization degree of PGBC with superior electrical conductivity is beneficial to the carrier transport and enhances the optoelectronic application of MoS<sub>2</sub>. In addition, the mass transfer by adsorption capacity of catalyst also makes great influences on photocatalytic activity, due to the surface reaction and short life of free radicals. Theoretically, the huge specific surface area and pore distribution of PGBC exhibit outstanding adsorption capacity to enhance the contact between pollutants and active species produced on the surface by attracting and collecting pollutants. MoS<sub>2</sub> as a photosensitive catalyst can utilize the light energy to mineralize the contaminants on or around the surface of the material, thereby restoring and improving the adsorption capacity of PGBC.

In the present work, we prepared PGBC through an efficient and green template-free route with potassium ferrate (K<sub>2</sub>FeO<sub>4</sub>) [14], which was used as both porous activating agent and catalyst for synchronous carbonization and graphitization of carbon precursor. On this basis, the incorporation of g-MoS<sub>2</sub> into PGBC was conducted to construct new-structure of g-MoS<sub>2</sub>/PGBC, in which PGBC plays the role of supporting and charge-mediator. Tetracycline hydrochloride (TC) with amphoteric behavior [37] is used as a representative of antibiotic pollutants for examining the co-catalytic effects of the as-prepared nanocomposite on photodegradation under visible-light irradiation. The main purposes of this research are to (1) synthesize g-MoS<sub>2</sub>/PGBC by simple operation and characterize its chemical structure, morphology, and optical properties; (2) explore the TC removal capacity containing adsorption and photodegradation, as well as the photocatalytic stability of the resulting photocatalyst in different solution medium with a series of operating conditions; and (3) discuss the removal pathways of TC by revealing the key adsorption mechanisms and predominant active species involved in photocatalytic process.

## 2. Materials and methods

### 2.1. Materials

Rice straw was obtained from bottomland of Dongting Lake wetland located in Hunan Province, China. Tetracycline hydrochloride (TC: purity > 98.5%), potassium ferrate (K<sub>2</sub>FeO<sub>4</sub>), sodium molybdate and thioacetamide were purchased from Shanghai Chemical Corp. and were

used without purification. Besides, deionized water (18.25 MΩ/cm) used in the experiment was produced by an Ulupure (UPRII-10 T) laboratory water system.

### 2.2. Preparation of photocatalyst

#### 2.2.1. Synthesis of PGBCs

The collected straw was washed repeatedly with deionized water to remove impurities, and then dried and shattered to a particle size of < 0.15 mm with sieving. Then, the straw powder was immersed and dispersed in aqueous 100 mL K<sub>2</sub>FeO<sub>4</sub> solution (0.1 M) with continuous stirring for 12 h. After vacuum dried at 80 °C overnight, the obtained solid mixture was transferred into a tube furnace operating at a continuous flow of N<sub>2</sub> gas and heated at a temperature of 900 °C for a residence time of 2 h at a heating rate of 5 °C/min. The carbonized black solids then underwent repeating pickling with diluted 1 M HNO<sub>3</sub> and deionized water for removal of residual inorganic impurities, which were denoted as PGBC after dried. Usual biochar was pyrolyzed by straw at 550 °C in N<sub>2</sub> atmosphere for 2 h without activation and graphitization.

#### 2.2.2. Synthesis of g-MoS<sub>2</sub>/PGBC

The PGBC obtained from the above steps was dispersed in 30 mL deionized water via ultrasonication for 15 min, and then mixed with 30 mL solution dissolved with 1 mmol of Na<sub>2</sub>MoO<sub>4</sub>·2H<sub>2</sub>O, 5 mmol of thioacetamide and 0.05 mmol polyethylene glycol (PEG 10,000), subsequently continued with the ultrasonication of 30 min. Then, the whole solution was transferred to a 100 mL Teflon-lined autoclave and went through hydrothermal treatment by heating up to 180 °C and lasting 24 h. After cooling to room temperature naturally, the solid precipitate generated in the solution was collected by centrifugation, followed by washing several times with anhydrous ethanol and deionized water. The black solid, undergone filtration and drying, was denoted as g-MoS<sub>2</sub>/PGBC<sub>x</sub> (x represents the theoretical mass ratio of PGBC to g-MoS<sub>2</sub>. If not specifically noted, the used composite in the experiment is g-MoS<sub>2</sub>/PGBC<sub>0.15</sub>).

### 2.3. Characterization methods

The surface morphology and elemental composition of the as-prepared g-MoS<sub>2</sub>/PGBC were characterized by field emission scanning electron microscope (SEM, JSM-6700 F, Japan) equipped with an energy dispersive X-ray analyzer (EDS, AMETER, USA) and transmission electron microscopy (TEM). The BET specific surface area and pore distribution characteristics were calculated according to the N<sub>2</sub> adsorption-desorption isotherms at 77.3 K using automatic surface and porosity analyzer (Quantachrome, USA). Fourier transform infrared spectrum (FT-IR) recorded in the range of 4000–400 cm<sup>-1</sup> was measured in KBr pellet by Nicolet 5700 Spectrometer, USA. The X-ray diffraction (XRD) patterns were obtained by Bruker AXS D8 Advance diffractometer with equipment of a Cu-Kα radiation source ( $\lambda = 1.5417 \text{ \AA}$ ) to investigate the crystal structures of as-synthesized material. Binding energies of the elements of sample were analyzed on basis of the X-ray photoelectron spectroscopy (XPS, Thermo Fisher Scientific-K-Alpha 1063, UK), with the calibration of C1 s at 284.8 eV. The Raman spectra were measured at ambient temperature by a Nanofinder 3.0 Raman spectrometer (Tokyo Instrument). The total organic carbon (TOC) assays were carried out using a Shimadzu TOC-VCPh analyzer. The UV-vis diffuse reflectance spectra (DRS) were recorded by the UV-vis spectrophotometer (Cary 300, USA) with an integrating sphere. Photoluminescence (PL) spectroscopy was monitored by a Hitachi-7000 fluorescence spectrometer.

### 2.4. Photoelectrochemical measurement

The photoelectrochemical examination of the as-prepared catalyst

was measured by a CHI 660D workstation in three-electrode cell, where regarded Pt electrode as the counter electrode and Ag/AgCl electrode as the reference electrode. In a typical procedure, the working electrode was made as follows: about 5 mg of the as-prepared photocatalyst was dispersed in 2 mL of 0.1% chitosan solution. The suspension was sonicated for 1 h and then dropped onto an FTO glass with an active area of 1.0 cm<sup>2</sup>. The electrode was dried at 50 °C overnight. Solution of 0.2 M Na<sub>2</sub>SO<sub>4</sub> was employed as supporting electrolyte as well as 300 W Xe lamp acting as light source in the experiments.

### 2.5. Evaluation of photocatalytic activity

The photocatalytic performance of the as-prepared composite was evaluated by the degradation of TC (20 mg/L) under visible light irradiation originated from 300 W Xe lamp with a cut off filter ( $\lambda > 420$  nm). In a typical process, 20 mg as-prepared composite was dispersed in an aqueous solution of TC (50 mL, 20 mg/L), and the whole solution was stirred for 60 min in the dark for achieving the adsorption-desorption equilibrium, which was used to calculate the adsorbed amount of TC. After that, the mixture solution was exposed to the 300 W Xe lamp with continues stirring, the samples were taken out and filtered using 0.22 μm PVDF disposable filters at each time interval (10 min), followed by analysis with UV spectrophotometer (UV-2550, SHIMADZU, Japan) and HPLC Series (Agilent, Waldbronn, Germany) at  $\lambda_{\text{max}}$  357 nm. The C-18 column (4.6 × 250 mm) was used and performed at the temperature of 30 °C with injection volume of 20 μL, and mobile phase was organic phase (acetonitrile: methanol = 2:1, v:v) with 0.01 mol/L oxalic acid at the flow rate of 1 mL min<sup>-1</sup>. For recycling experiment, the used catalyst was collected by filtration, and then was used for another run undergone washing and drying to test the stability of the composite.

## 3. Results and discussion

### 3.1. Characterization of g-MoS<sub>2</sub>/PGBC

The morphologies and microstructures of the as-prepared materials were characterized by SEM and TEM. The resulting particles of PGBC are found to be consisted of plentiful thin-walled carbon hollow microtubules with abundant pores on the carbon wall as shown in Fig. 1a, which is inherited from the natural morphology of straw. Retaining the hollow elongated framework, on one hand, is conducive to offer pathways for electrolyte uptake and provide conductive channels for rapid electron transport. On the other hand, the PGBC posing smooth structure and abundant pore is a suitable platform for decorating g-MoS<sub>2</sub> to avoid the severe aggregation of nanosheets. As displayed in Fig. 1c, curved edged g-MoS<sub>2</sub> nanosheets grow disorderly on the tubular carbon wall after hydrothermal reaction, which may be closely related to the interaction between the functional groups of carbonaceous material and Mo<sup>4+</sup> of precursors [38,39]. Transmission electron microscopy (TEM) analysis of composite proves a very close contact between g-MoS<sub>2</sub> and PGBC, in which the carbonaceous material serves as a supporter for the g-MoS<sub>2</sub> nanosheets. The high-resolution TEM (HRTEM) images of nanocomposite, shown in Fig. 1e and f, demonstrate both interplanar spacings of 0.35 nm and 0.65 nm, indicating that the characteristic lattice fingers of PGBC and g-MoS<sub>2</sub> are identified, respectively.

Further information on the pore structural properties of the synthesized materials was received from adsorption-desorption isotherm measured at 77 K. As can be seen from part a of Fig. 2, the g-MoS<sub>2</sub>/PGBC exhibits I/IV-type isothermal curves, and there is a relatively abrupt adsorption inflection at low relative pressures, indicating the existence of a considerable number of micropores. Moreover, the small hysteretic loop of desorption branch extending from  $P/P_0$  at 0.5 to 0.9 demonstrates the presence of a moderate number of mesopores. The calculated pore-size distribution using the BJH method and desorption data indicates that the g-MoS<sub>2</sub>/PGBC contains an average pore size of

2.13 nm, with most of the pores concentrating in the size range of 0.5–30 nm. Concerning to the TC molecule dimension, the g-MoS<sub>2</sub>/PGBC with appropriate pore-size distribution is endowed with efficient adsorption capacity to TC molecular [37]. On the whole, the BET surface area of g-MoS<sub>2</sub>/PGBC is calculated to be 266.8 m<sup>2</sup>/g and the total pore volume estimated by BJH desorption isotherm is 0.126 cm<sup>3</sup>/g, with the plenty of mosaic folded edges structure of MoS<sub>2</sub> nanosheets like the wings.

Wide-angle X-ray diffraction of PGBC shows peaks at 26.1° and 44.2°, which are characteristic of representative (002) and (101) reflections of graphitic carbon [16,40]. While for g-MoS<sub>2</sub>/PGBC shown in Fig. 2b, other detected peaks appearing in 32.5° and 57.8° can be indexed to the (100) and (110) planes of hexagonal phase in MoS<sub>2</sub> (JCPDS card No. 37-1492) [41]. Compared with bulk MoS<sub>2</sub>, the disappeared (002) reflection implies the presence of fewer layers of g-MoS<sub>2</sub> [42]. The weaker and broader peak of graphite (002) could be observed in diffraction of g-MoS<sub>2</sub>/PGBC because of its weaker crystallization resulting from the destruction in hydrothermal process, also suggesting the dispersion of the g-MoS<sub>2</sub> clusters on the PGBC surface.

Raman spectroscopy was further applied to identify the composite production. The graphitic structure of PGBC is observed on Fig. 2c, and the spectrum displays two evident peaks at 1350 cm<sup>-1</sup> corresponding to the D band and 1583 cm<sup>-1</sup> corresponding to G band, respectively. Typically, the D band is ascribed to the defect sites or disordered structure in carbon-containing materials, while the G band is arisen from the stretching vibration of sp<sup>2</sup>-hybridized carbon of graphite. In addition, another obvious peak at 2710 cm<sup>-1</sup> corresponds to the 2D band, indicating there is hexagonal symmetry in the graphitic carbon [40,43]. The integral intensity ratio of D band to G band ( $I_D/I_G$ ), an identifier for determining the degree of crystallization of carbon materials, is calculated to be 1.08, confirming the PGBC is provided with a considerable degree of graphitization. The g-MoS<sub>2</sub>/PGBC sample demonstrates similar peaks at the corresponding position: 1350 cm<sup>-1</sup> (D band), 1585 cm<sup>-1</sup> (G band), and, 2720 cm<sup>-1</sup> (2D band), implying the presence of PGBC. Besides, two characteristic peaks of g-MoS<sub>2</sub> that corresponded to the E1 2g and A<sub>1g</sub> vibration modes, respectively, are observed at 377 cm<sup>-1</sup> and 402 cm<sup>-1</sup> in the local amplification of g-MoS<sub>2</sub>/PGBC spectrum [24,44], further verifying the successful synthesis of the g-MoS<sub>2</sub>/PGBC with no substance change in g-MoS<sub>2</sub> and PGBC. The increased  $I_D/I_G$  ratio of g-MoS<sub>2</sub>/PGBC is estimated to be 1.13, which is attributed to the further production of defect and edge through the hydrothermal process. Although the  $I_D/I_G$  intensity ratio is higher than that before modification due to the hydrothermal reaction, the  $I_D/I_G$  value of 1.13 still indicates that the relatively high degree of graphitization and good electronic conductivity of the g-MoS<sub>2</sub>/PGBC.

Surface analysis about the chemical composition and valence state of the elements in manufactured products was performed using X-ray photoelectron spectroscopy. In comparison with the survey spectrum of PGBC before and after modification (Fig. 2d), besides the extra introduction of Mo and S elements in g-MoS<sub>2</sub>/PGBC, the proportion of oxygen is observed to increase from 7.94 to 14.62 at%, implying there are more oxygen-containing functional groups on composite surface, which is beneficial to promoting the generation of active free radical during catalysis as a result of the electron-transfer mediator of oxygen functional groups in composite [45]. In the C 1 s XPS spectrum of g-MoS<sub>2</sub>/PGBC (Fig. 3a), the C 1 s band can be resolved into three peaks located at 284.20, 285.90, and 286.65 eV, referring to the binding of C sp<sup>2</sup>, C=C/C=O, and MoC=O, respectively. There are also three fitted peaks in O 1 s spectrum positioned at 531.10, 532.66 and 533.28 eV, which may assign to C=O, C—O/H—O, and Mo—O bonds, respectively. Fig. 3c shows the binding energies of Mo 3d peaks, corresponding to the 3d<sub>3/2</sub> and 3d<sub>5/2</sub> orbit of Mo<sup>4+</sup> which were found at 232.10, and 230.12–228.90 eV. Furthermore, two broad peaks centering at 235.85 and 233.02 eV are characteristic of the 3d<sub>3/2</sub> and 3d<sub>5/2</sub> orbit of oxidation state Mo<sup>6+</sup>, which may be caused by the slight partial oxidation of Mo atoms at the defects or edges of MoS<sub>2</sub> with high oxidation activity [46].

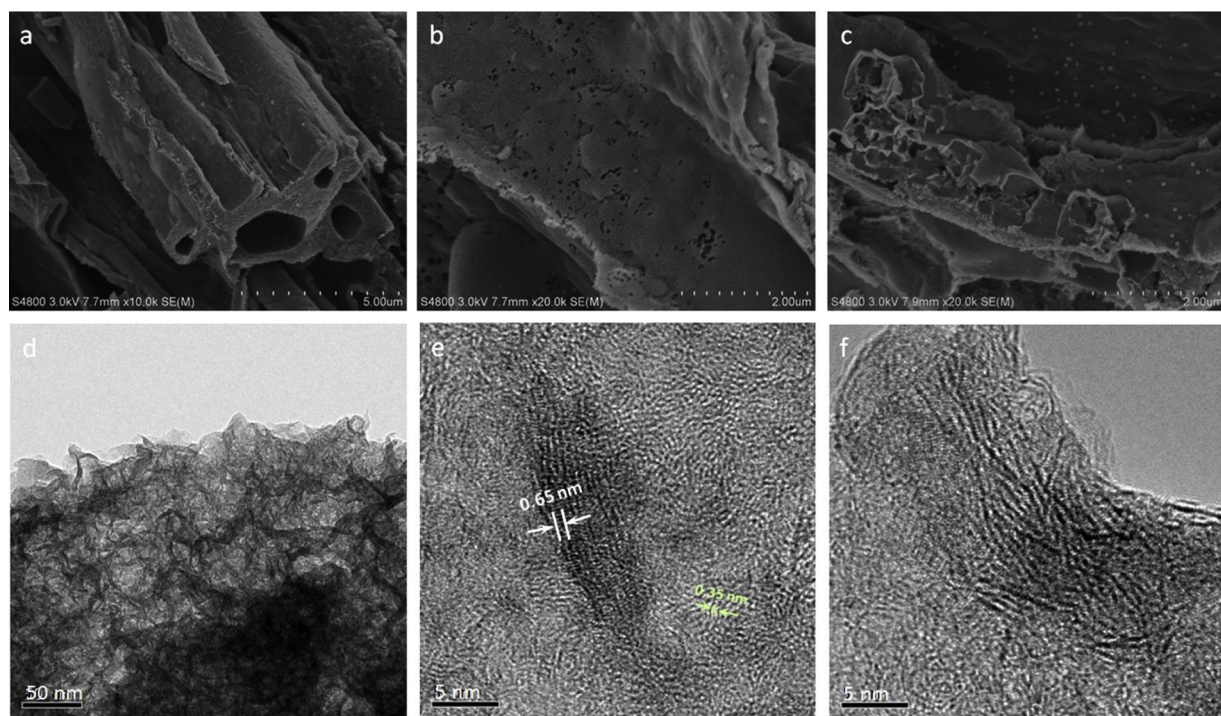


**Fig. 1.** SEM images of pristine porous graphitic carbon biochar (a and b) and g-MoS<sub>2</sub>/PGBC (c), TEM image of g-MoS<sub>2</sub>/PGBC (d), and HRTEM images of g-MoS<sub>2</sub>/PGBC (e and f).

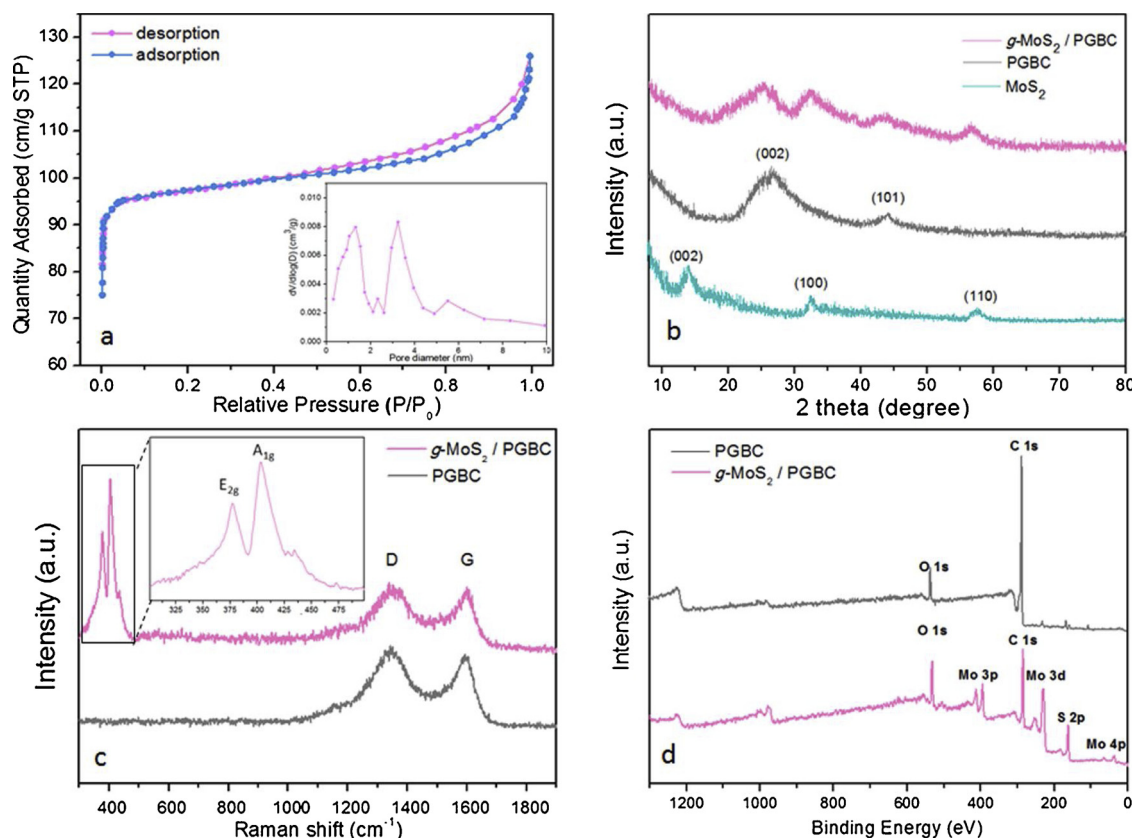


**Fig. 2.** The N<sub>2</sub> adsorption-desorption isotherms of g-MoS<sub>2</sub>/PGBC at 77 K, inset shows the pore-size distribution curve of g-MoS<sub>2</sub>/PGBC (a); XRD patterns of pure MoS<sub>2</sub>, PGBC and g-MoS<sub>2</sub>/PGBC (b); Raman spectra of pure MoS<sub>2</sub>, and g-MoS<sub>2</sub>/PGBC and local amplification of g-MoS<sub>2</sub>/PGBC spectrum (c); XPS survey spectra of porous graphitic carbon biochar and g-MoS<sub>2</sub>/PGBC (d).

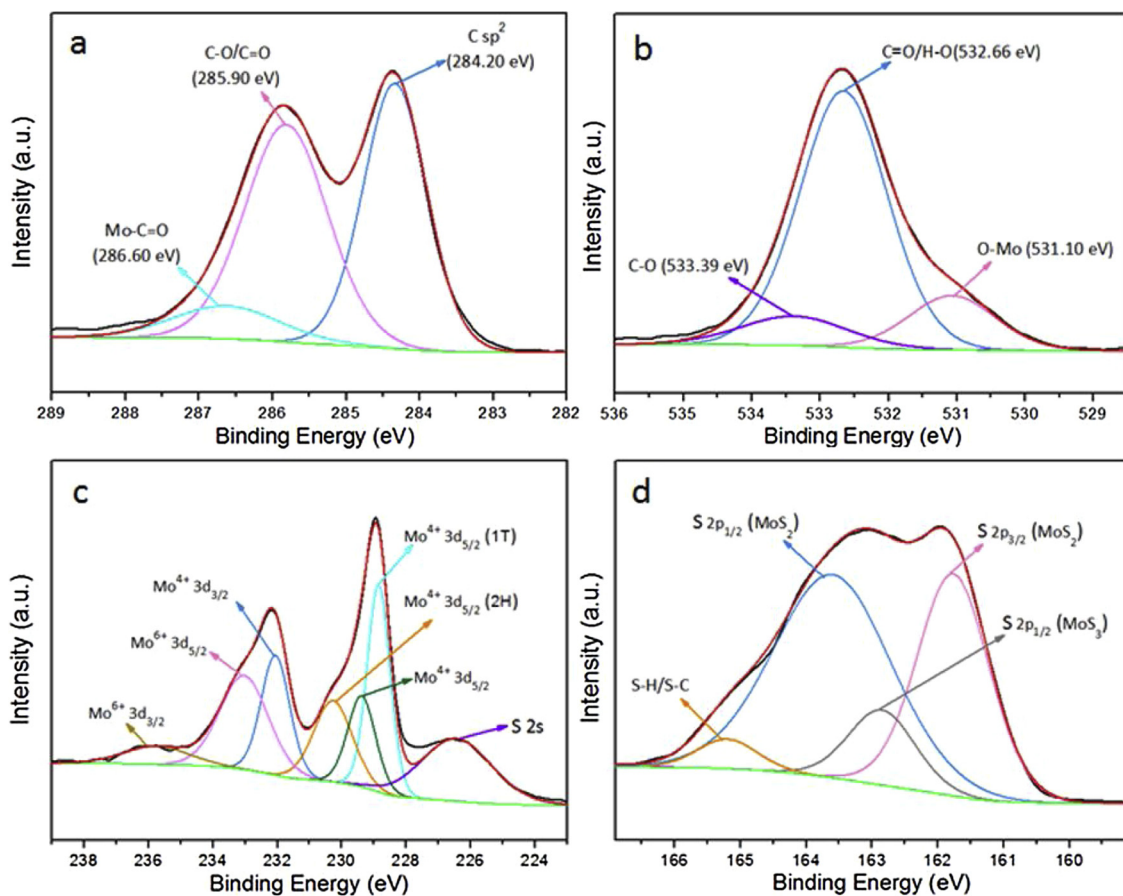


Fig. 3. High resolution XPS spectrum of C 1 s (a), O 1 s (b); Mo 3d (c); and S 2p (d) in g-MoS<sub>2</sub>/PGBC.

The high-resolution XPS spectrum of S 2p is fitted and showed in Fig. 3d, and the peaks located at 163.20 and 161.80 eV, respectively, are attributed to the doublet S 2p<sub>1/2</sub> and S 2p<sub>3/2</sub>, characterizing of S<sup>2-</sup> in g-MoS<sub>2</sub>. Taking another analysis of peak at 226.50 eV (Fig. 3c) arising from S 2s into account, the present of MoS<sub>2</sub> in the sample is verified.

### 3.2. Optical properties and photo-electrochemical characteristics

The optical absorption properties and bandgap of the as-prepared samples were studied by the comparison of the UV/vis diffuse reflectance spectrum (DRS), as shown in Fig. 4a. Pure MoS<sub>2</sub> shows a considerably broad absorption band having a characteristic edge at around 680 nm, which could be used to calculate the bandgap value as 1.82 eV. After the incorporation of PGBC, increased optical absorption intensity and a little broad spectral response in visible light wavelength of g-MoS<sub>2</sub>/PGBC are obtained. This slight improvement of visible light response may be due to the formation of the Mo-S-C bond which forms an energy level hybridization between g-MoS<sub>2</sub> and PGBC [47]. The inset of Fig. 4a describes the plot of (chv)<sup>n</sup> (bulk MoS<sub>2</sub> is an indirect band gap semiconductor ( $n = 1/2$ ); g-MoS<sub>2</sub> is a direct band gap semiconductor ( $n = 2$ )) versus photon energy ( $h\nu$ ) [48], which is performed to determine the optical band gap optimizing from 1.82 to 1.91 eV when hierarchical g-MoS<sub>2</sub> integrated with PGBC. The results infer that the cooperative effect between g-MoS<sub>2</sub> nanosheets and PGBC would extend the adsorption region towards visible light and allow a more efficient utilization of solar energy, which leads to more photo-generated electron-hole pairs for the photocatalysis. In addition, the synthesized nanocomposite has a higher redox potential for free radical generation and contaminant degradation by holes with stronger oxidation ability.

The photoluminescence (PL) emission spectra were performed to

reveal the charge carrier transfer and recombination efficiency of as-fabricated semiconductor photocatalyst, since the secondary recombination between photo-generated carriers is accompanied by fluorescence emission. It is commonly known that the stronger intensity of the fluorescence arises from the recombination of electrons and holes indicates the shorter lifetime of the photo-generated charge carriers [49]. Pure MoS<sub>2</sub> possesses a high recombination rate of carriers with strong PL intensity which decreases the photocatalytic ability. As presented in Fig. 4b, the PL intensity of g-MoS<sub>2</sub>/PGBC is found to be greatly lower compared with that of pure MoS<sub>2</sub>, demonstrating the introduction of PGBC as carrier mediator can effectively accelerate the transfer and separation of electron-hole pairs and thereby prevent the recombination of charge carriers. Consequently, stronger photocatalytic performance of g-MoS<sub>2</sub>/PGBC is achieved by the enhanced electron utilization efficiency.

The improved charge separation behavior was further confirmed by the transient photocurrent response experiments under periodic visible light on/off (Fig. 4c). The photocurrent density of g-MoS<sub>2</sub>/PGBC is intensively enhanced, and its value is over twice higher than that of pristine MoS<sub>2</sub>, suggesting that the modification by PGBC supporting can make a remarkable improvement in suppressing the recombination of photoinduced electrons and holes generated by MoS<sub>2</sub>. Moreover, the surface resistance of semiconductor is one of the important factors affecting the photocatalytic property of catalyst, which could be provided from Nyquist impedance plots in EIS measurement based on the diameter of the semicircle corresponding to the carrier transfer resistance, where a smaller arc radius manifests a lower transfer resistance of the composite and further means higher efficiency in charge transfer on catalyst surface. The Nyquist plots for the samples in Fig. 4d show that g-MoS<sub>2</sub>/PGBC possesses smaller surface resistance than that of pristine MoS<sub>2</sub>, indicating the faster separation and rapid transfer of the

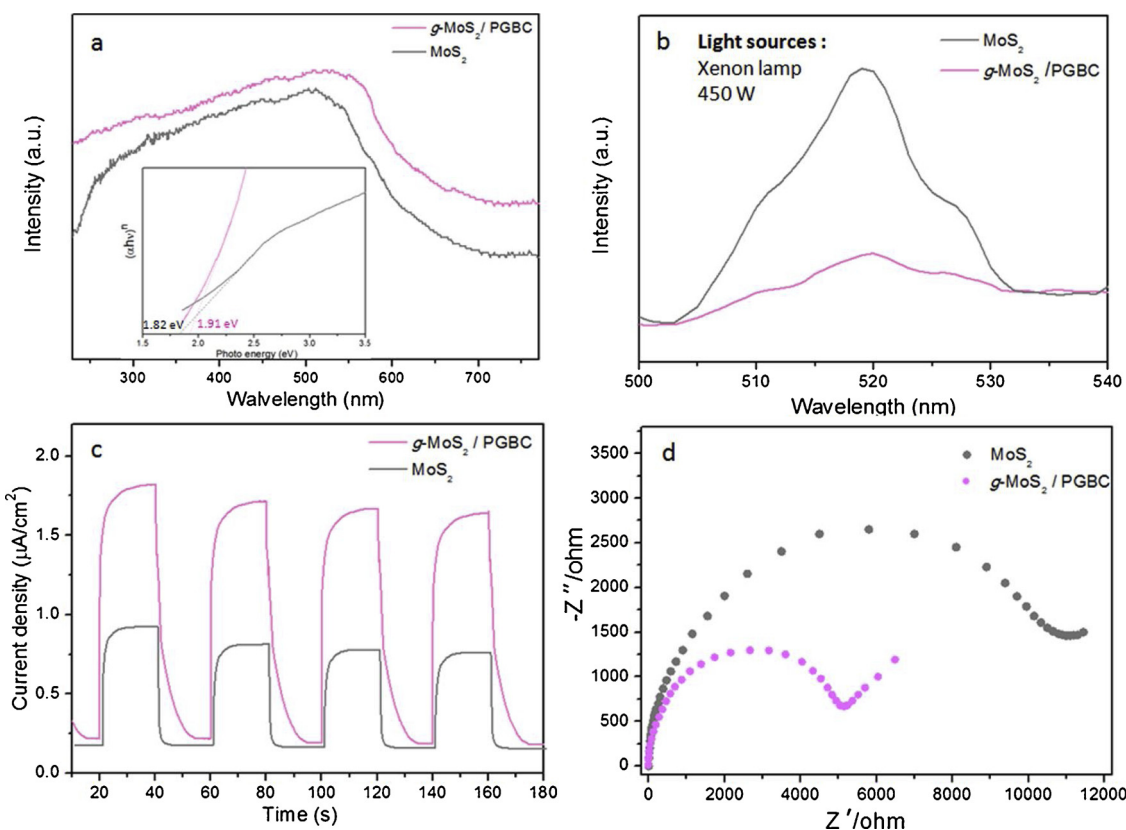


**Fig. 4.** UV-vis diffuse reflectance spectra and the plots of  $(\alpha h v)^n$  vs photon energy ( $h v$ ) of as-prepared  $\text{MoS}_2$  and  $\text{g-MoS}_2/\text{PGBC}$  (a); Photoluminescence (PL) spectra (b); transient photocurrent response (c); and electrochemical impedance spectra (d) for the as-prepared samples.

photogenerated charge carriers during the photocatalytic reaction process. These results can be implied to the fact that PGBC as a charge mediator can facilitate carrier transfer to achieve effective separation of electron-hole pairs, on the basis of its interconnected structures and excellent electrical conductivity. The above views are in good consistent with the observation of photocatalytic activity.

### 3.3. Adsorption and photocatalytic properties

It is well established that adsorption ability of a photocatalyst towards the target pollutants is one of the decisive factors affecting the photocatalytic efficiency. The adsorption capacity of the prepared composites for TC molecules was investigated under darkness and shown in Fig. 5. It is observed that the  $\text{g-MoS}_2/\text{PGBC}$  exhibits relatively large adsorbed amount of TC when the adsorption equilibrium is reached after 1 h. Attributed to the surface hydrophobicity, large specific surface area, suitable pore structure and attractive surface charge on PGBC, adsorption capacity of the obtained sample is enhanced with increasing PGBC content. The pseudo-first-order, pseudo-second-order models were used to analyze the adsorption kinetics of TC molecules by  $\text{g-MoS}_2/\text{PGBC}$ . On the basis of the values of correlation coefficient (Table S1), it can be concluded that pseudo-second-order model is more suitable to describe the adsorption behavior of TC, indicating the TC adsorption is much affected by chemical mechanism. It is worthwhile mentioning that the highest rate constants ( $k_2$ ) is received from experiment of  $\text{g-MoS}_2/\text{PGBC}_{0.15}$ . Undergone adsorption-desorption equilibrium within 1 h dark reaction, all samples were exposed to visible light, as presented on Fig. 5e. Compared with the negligible TC removal on control and pure  $\text{MoS}_2$  alone, successful combination of  $\text{g-MoS}_2$  and PGBC in the constructed nanocomposite is likely to inspire the improvement of photocatalytic ability. To shed light on the quantitative characterization of TC degradation kinetics, the experimental data were linear fitted by  $\ln(C_0/C) = kt$  [39]. As shown in Fig. 5f, the  $k$  denoted

the degradation rate constant is found to the largest value of  $0.0216 \text{ min}^{-1}$  in treatment of  $\text{g-MoS}_2\text{-PGBC}_{0.15}$ , revealing a reasonable and efficient composition ratio between PGBC and  $\text{g-MoS}_2$  with the co-effects in enhancing the adsorption activity and suppressing the photo-induced electron-hole pairs recombination in photocatalytic system, and the nanocomposite of  $\text{g-MoS}_2/\text{PGBC}_{0.15}$  was used in subsequent experiments (According to the result obtained by the EDS (Fig. S1) that is consistent with XPS analysis, the content of  $\text{MoS}_2$  in the synthesized nanocomposite is estimated to be about 25 wt.%). In addition, by comparing the usual biochar as the substrate modified with  $\text{MoS}_2$ , it can be observed that the  $\text{MoS}_2/\text{BC}_{0.15}$  has a relatively good adsorption capacity. Although its specific surface area is less than  $\text{g-MoS}_2/\text{PGBC}_{0.15}$ , the functional groups and defects on  $\text{MoS}_2/\text{BC}_{0.15}$  surface are treated as adsorption sites. However, the photocatalytic degradation of the  $\text{MoS}_2/\text{BC}_{0.15}$  is very weak, which can be attributed to the poor electron conductivity of the unactivated biochar and the serious stacking of  $\text{MoS}_2$  (Fig. S2).

Effects of initial concentrations on TC removal were also investigated and shown on Fig. 6a. On the whole, the synthesized  $\text{g-MoS}_2/\text{PGBC}$  has good TC removal efficiency with initial pollutant concentration in the range of 10 to 50 mg/L, which is attributed to its relatively excellent adsorption performance. Fig. 5d confirms that higher equilibrium adsorbed amount of TC is obtained from higher initial concentration due to the more powerful driving force to overcome the mass transfer resistances between liquid and solid phases [37,46]. The adsorption equilibrium data at darkness were fitted by Langmuir, Freundlich models with the good correlation coefficients ( $R^2$ ) of 0.9958 and 0.9817 (Table S2), respectively. This result implies that the TC adsorption onto  $\text{g-MoS}_2/\text{PGBC}$  is mostly the monolayer formation relevant to the functions of chemical mechanism, while the physical interaction is also involved in the adsorption to form adsorbate multilayers [42,50]. Several critical parameters (Table S2) obtained from the fitting models suggest that the TC adsorption process by  $\text{g-MoS}_2/\text{PGBC}$

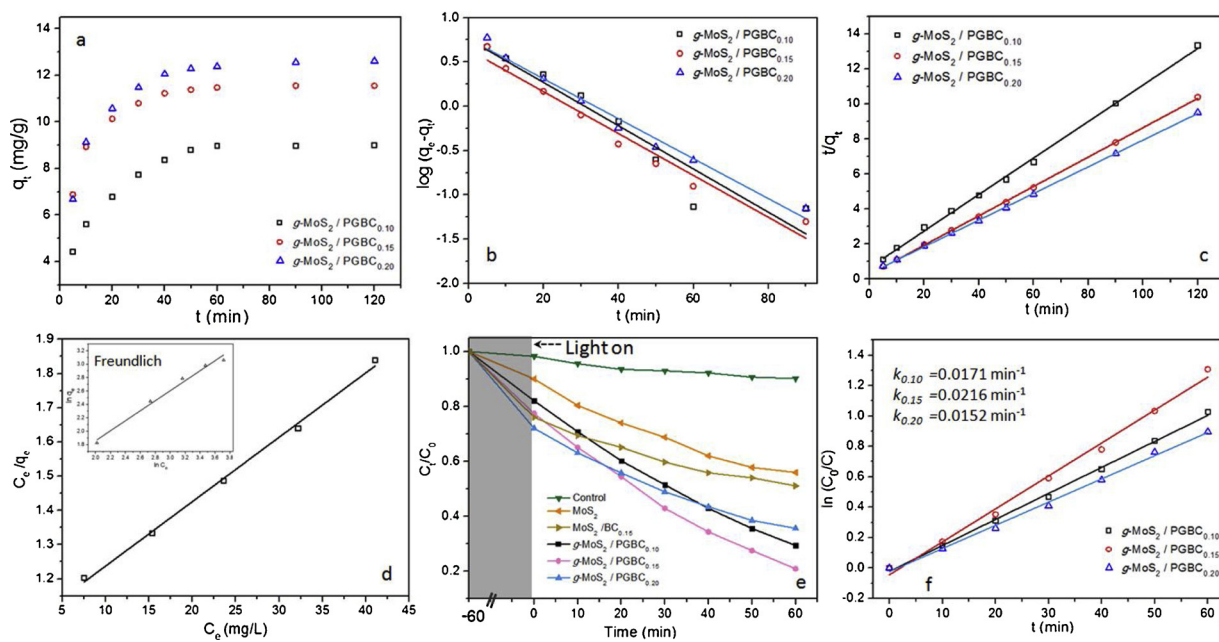


**Fig. 5.** Effect of contact time on the adsorption of TC onto g-MoS<sub>2</sub>/PGBC under darkness (a); the pseudo-first-order plots (b); pseudo-second-order plots (c); detail equilibrium isotherms: (d) Langmuir model and Freundlich model (inset) for TC adsorption by g-MoS<sub>2</sub>/PGBC under darkness; removal of TC in the presence of different photocatalysts with various composition ratios between g-MoS<sub>2</sub> and PGBC under visible light irradiation (e); photocatalytic rate of g-MoS<sub>2</sub>/PGBC under visible light irradiation (f).

is facile and favorable. However, the photodegradation rate of TC shows a negative trend as initial TC concentration increased (Table 1), which can be ascribed to the decreased photon absorption caused by less active sites with more attached pollutants on the surface of g-MoS<sub>2</sub>/PGBC, as well as the reduced path length of photon entering the

solution) [33].

The influences of initial pH on TC removal are presented on Fig. 6b, which are originated from the processes of both pollutant adsorption and catalytic degradation. There is no denying that pH level plays an important role in the surface charges on the material and the existing

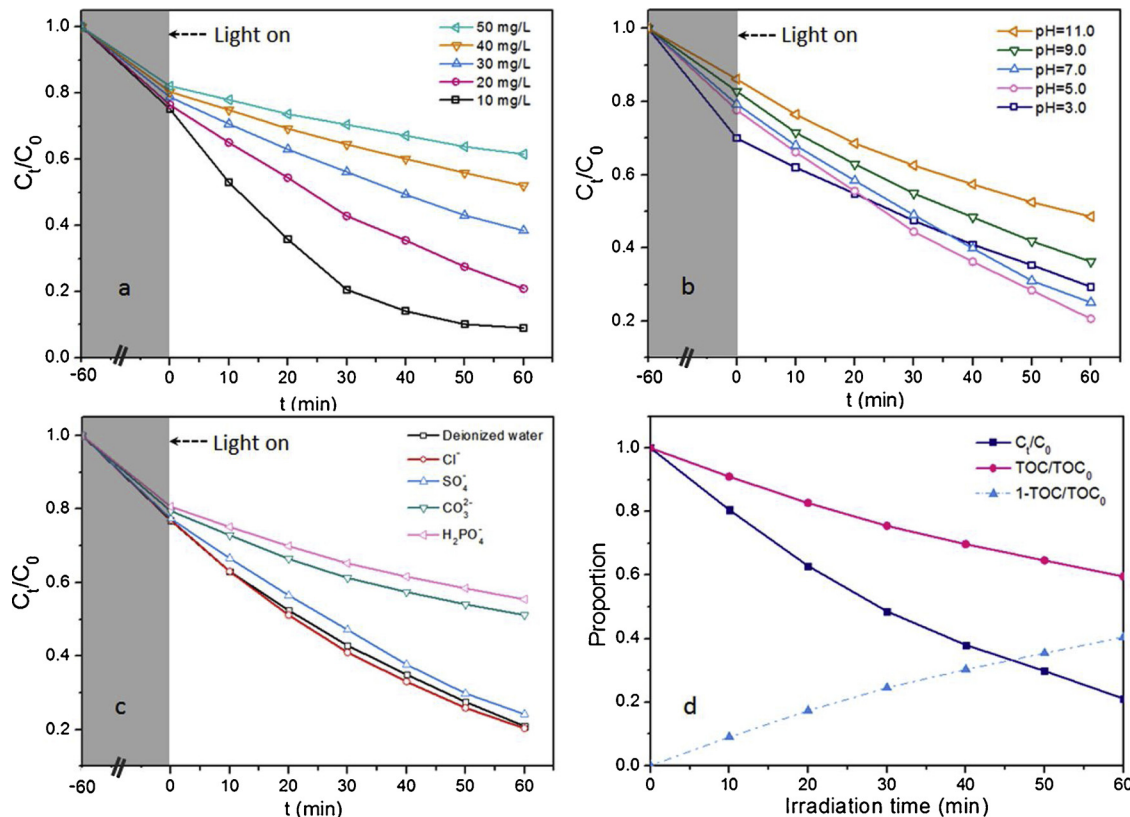


**Fig. 6.** Effect of initial TC concentrations (a); initial pH (b), and coexisting anions (c) on the degradation of TC over g-MoS<sub>2</sub>/PGBC; the photodegradation and TOC removal curves (d) of TC on g-MoS<sub>2</sub>/PGBC under visible light irradiation.

**Table 1**

The pollutant degradation rate constants in different initial TC concentration by  $g\text{-MoS}_2/\text{PGBC}$  under light irradiation.

Initial TC concentration (mg/L)	10	20	30	40	50
Degradation rate ( $k$ ) (min <sup>-1</sup> )	0.0378	0.0216	0.0121	0.0073	0.0049
$R^2$	0.9923	0.9986	0.9998	0.9968	0.9966

forms of pollutants. According to the results of Zeta potential measurement (Fig. S3),  $g\text{-MoS}_2/\text{PGBC}$  surface shows electronegative and decreases gradually with increasing pH value in a range of 3.0–11.0. Based on the different dissociation constant of tetracycline ( $pK_a = 3.4, 7.6$  and 9.7) [51], TC molecules exist in solution with different forms of cation ( $\text{TCH}_3^+$ ), zwitterions ( $\text{TCH}_2^+$ ) and anions ( $\text{TCH}^-$  and  $\text{TC}^{2-}$ ) derived from the protonation and deprotonation of multiple ionizable functional groups. In the dark reaction, the maximum adsorption of TC molecule occurs at a pH of 3.0 by electrostatic attraction, while the negatively charged surface of nanocomposite presents an enhanced electrostatic repulsion to anions  $\text{TCH}^-$  and  $\text{TC}^{2-}$  when pH value is greater than seven. There is a somewhat surprising result that a low catalytic degradation rate of TC is observed under acidic condition, which may arise from the fact that excessive adsorbed TC molecules might occupy the active site and prevent light from reaching the catalyst surface [35], further hindering the hole-electron photoexcitation process. In addition, strong electrostatic repulsion under strong alkaline conditions leads to a decrease in free radical generation due to less hydroxide ions and  $\text{TC}^{2-}$  reaching the catalyst surface, followed by a decrease in photocatalytic ability.

To further explore the practical application of the prepared nanocomposite, the most common anions in natural water containing  $\text{Cl}^-$ ,  $\text{SO}_4^{2-}$ ,  $\text{H}_2\text{PO}_4^-$ , and  $\text{CO}_3^{2-}$  were discussed for their effects on the adsorptive-catalytic reaction process for TC. Since  $\text{Na}^+$  ions have been proven to show little effect on the removal of TC [37], all of the above anionic with form of sodium salts at 10 mM concentration were used to explore the influences of ion interference. Fig. 6c displays the different TC removal rates in the presence of various anions in order of  $\text{Cl}^- > \text{SO}_4^{2-} > \text{CO}_3^{2-} > \text{H}_2\text{PO}_4^-$ . A slight enhancement could be found within NaCl electrolyte, which may be explained by the scavenging reaction of the photo-induced holes and  $\text{Cl}^-$ , resulting in more effective separation of hole-electron pairs [47]. The coexistence of  $\text{CO}_3^{2-}$  or  $\text{H}_2\text{PO}_4^-$  in TC solution exhibits considerable inhibition in both adsorption and photocatalytic degradation processes. They are regarded as pH buffers and can alkalinize the solution to a certain extent, leading to decrease in TC adsorption on  $g\text{-MoS}_2/\text{PGBC}$  surface by electrostatic repulsion at darkness. Moreover,  $\text{H}_2\text{PO}_4^-$  might serve as a chelating agent and attach to the catalyst surface, covering some active sites [52]. In terms of the radical generation, it is well established that  $\text{CO}_3^{2-}$  and  $\text{H}_2\text{PO}_4^-$  are two typical free radical scavenger, the free radicals produced at the composite surface are captured immediately by the coexisting  $\text{CO}_3^{2-}$  and  $\text{H}_2\text{PO}_4^-$  [47], contributing to decline in the photocatalytic activity.

Complete mineralization capacity of photocatalyst towards organic pollutants is a crucial parameter in the actual application, because deep mineralization of organic pollutant into water and carbon dioxide is environmentally friendly and harmless [10]. The total organic carbon (TOC) removal by the as-prepared composites is used as an indicator to measure the degree of mineralization, as shown in Fig. 6d. It could be found that more than 40% of TOC could be removed after 60 min irradiation, which accounts for nearly half of the TC decomposition with favorable mineralization capability.

#### 3.4. Photocatalyst recyclability and its application on real water samples

In order to deeply investigate the practical application of papered composites in actual natural water, river water and tap water

(characteristics shown in Table. S3) were applied as the medium of TC solution in comparison with deionized water, since initial water status might also influence the photocatalyst application. As can be seen from Fig. 7a, both adsorption process and photodegradation process have different responses in various medium. Due to the difference in pH between deionized and tap water, the adsorbed amount of TC by  $g\text{-MoS}_2/\text{PGBC}$  in tap water is slightly lower than that in lab single system of deionized water. However, higher adsorption of TC is observed in the medium of river water, which could be explained by (1) wrapping and cross-linking effect of the flocs, (2) additional adsorption derived from fine particles, and (3) bridging role of coexisting metal ions between material surface and TC molecules. As far as the degradation process is concerned, there is a competitive relationship between the organic matter contained in the river water and TC molecules. Besides, the coexisting anions including  $\text{CO}_3^{2-}$ ,  $\text{H}_2\text{PO}_4^-$  and  $\text{SO}_4^{2-}$  would capture and consume the photo-generated free radicals, further inhibiting the degradation of TC.

The recycling experiments were performed under the same condition to evaluate the reusability and stability of the as-prepared composites. As presented on Fig. 7a, there is no significant decrease in removal efficiency of TC over  $g\text{-MoS}_2/\text{PGBC}$  after 3 cycles, regardless of the type of solution medium, and the as-prepared nanocomposite maintains nearly 70% TC removal efficiency in actual water cycle treatment. Comparing the XRD spectrum before and after catalytic degradation (Fig. S4), it could be found that the crystal structure of composite remains basically unchanged, indicating the high stability of  $g\text{-MoS}_2/\text{PGBC}$  during photocatalysis process. Taking the above observations into account, as well as the comparison on photocatalytic activity of different typical related catalysts (Table. S4), it can be demonstrated that the  $g\text{-MoS}_2/\text{PGBC}$  as a highly efficient, green, sustainable photocatalyst possesses a long-term application potential for wastewater remediation.

#### 3.5. TC removal mechanisms by $g\text{-MoS}_2/\text{PGBC}$

It is well established that the efficient photocatalytic degradation needs handle both the mass transfer and light transfer issues. The adsorption capacity of photocatalyst for TC is a decisive factor in photodegradation. It is obvious that the electrostatic interaction involves in the adsorption process based on the discussion about effect of pH on TC adsorption. It can be observed by comparing the FT-IR spectrum of  $g\text{-MoS}_2/\text{PGBC}$  before and after adsorption (Fig. S5), the peaks at 2366, 1632, 1443 cm<sup>-1</sup> assigned to the stretching vibration of cumulated double bond, C=O, and aromatic benzene ring skeleton, respectively, shift in varying degrees due to the  $\pi\text{-}\pi$  conjugate effect between benzene ring, double bonds on  $g\text{-MoS}_2/\text{PGBC}$  and aromatic compound of TC, confirming the mechanism of  $\pi\text{-}\pi$  stacking interaction. The S–H and O–H vibration at 667 cm<sup>-1</sup> and around 3384–3450 cm<sup>-1</sup>, respectively, move to lower absorbance areas upon adsorption, which can be attributed to the hydrogen bonding interaction between TC molecule and these functional groups, since the unsaturated sulfur bonds at the edges are highly reactive. Besides, the appropriate pore-size distribution makes  $g\text{-MoS}_2/\text{PGBC}$  become a tailor-made adsorbent for pore-filling of TC by partition effect.

The photodegradation mechanisms mainly involve active species with strong oxidizing being explored by free radical trapping experiment. Three kinds of typical reagent, 1,4-benzoquinone (BQ), isopropanol (IPA), and ethylenediaminetetraacetic acid disodium (EDTA-2Na) were adopted as the scavengers of superoxide radical ( $\text{O}_2^-$ ) hole ( $\text{h}^+$ ), and hydroxyl radical ( $\cdot\text{OH}$ ), respectively, to consume the reactive species and further decline the photocatalytic performance. Obviously, Fig. 7b depicts that the degradation efficiency of TC evidently drops to 33.63% after EDTA-2Na addition, indicating the active species of holes play a key role towards TC degradation. In addition, a nearly half decrease of degradation percentage could be found within the present of IPA, illustrating that the  $\cdot\text{OH}$  also contributes to TC degradation to a

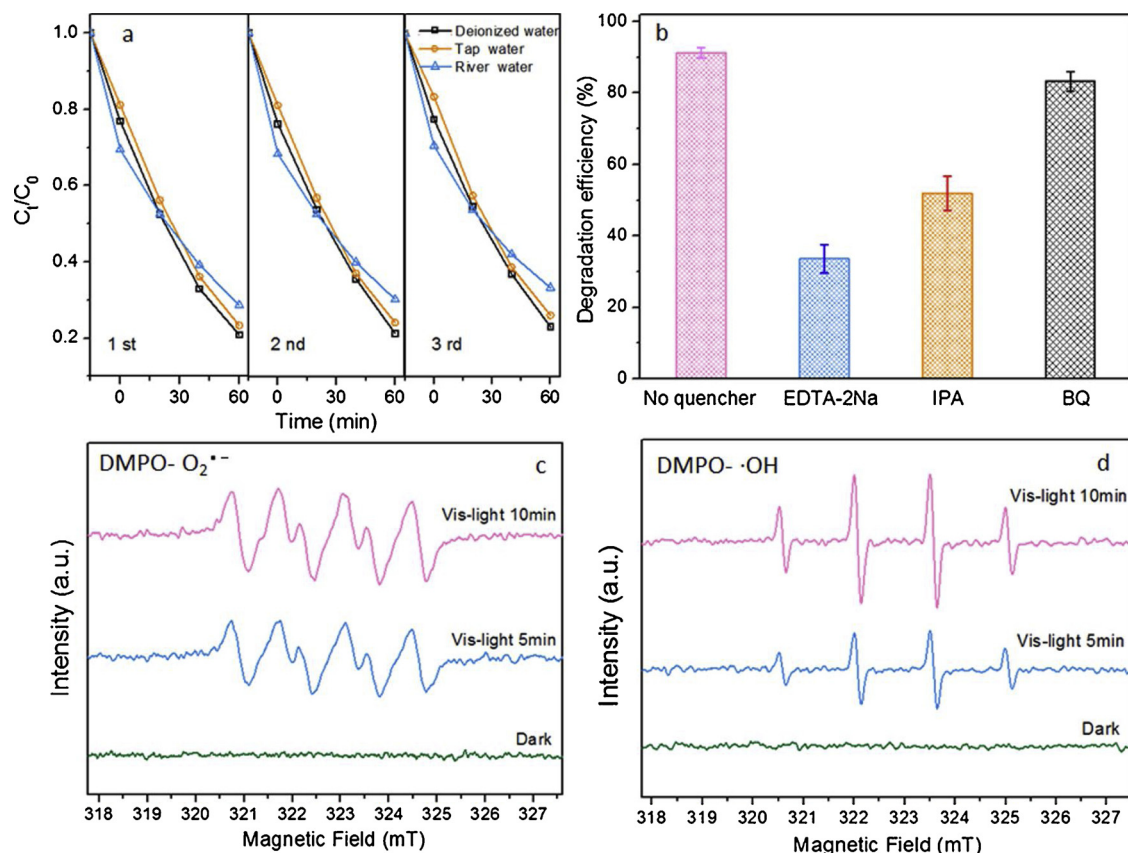


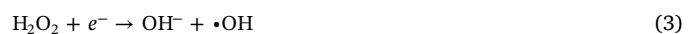
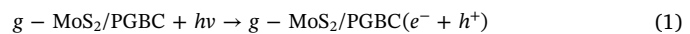
**Fig. 7.** Cycling performance of photocatalytic degradation for TC removal in different water samples (a); degradation curves of TC with additions of scavengers over *g*-MoS<sub>2</sub>/PGBC under visible light (b); and ESR spectra of radical adducts trapped by DMPO in *g*-MoS<sub>2</sub>/PGBC dispersion under dark and visible light irradiation: in methanol dispersion for DMPO-·O<sub>2</sub><sup>−</sup> (c); in aqueous dispersion for DMPO-·OH (d).

certain extent. However, when adding a screening agent of ·O<sub>2</sub><sup>−</sup> (BQ), the degradation efficiency of TC is depressed a little, which implies there are superoxide radicals participated but shown minor factor in TC degradation. Notably, all results depict the photocatalytic degradation of TC mainly relies on h<sup>+</sup>, followed by ·OH, while ·O<sub>2</sub><sup>−</sup> has minimal effect.

To gain more insight, the Electron Paramagnetic Resonance (ESR) spin-trap with DMPO was performed to further validate the above-obtained reactive oxidative species generated in this photocatalytic system over *g*-MoS<sub>2</sub>/PGBC under visible irradiation. Fig. 7c and d display the EPR spectra obtained under dark and irradiation, and indicate firstly no radicals are generated under dark, which confirms that the relatively high TC removal before illumination is derived from the excellent adsorption capacity of the nanocomposite. The obvious quartet peaks with intensity ratio of 1:2:2:1 could be detected in *g*-MoS<sub>2</sub>/PGBC + VL (visible light) photocatalytic system, which is ascribed to the spectral characteristic signal of DMPO-OH, demonstrating that ·OH with high oxidation activity occurs in TC degradation process. Meanwhile, a typical six-peak signal of DMPO-·O<sub>2</sub><sup>−</sup> is observed by enhancing with visible light irradiation. ESR analysis indicates that ·OH and ·O<sub>2</sub><sup>−</sup> as the active species are indeed produced in photocatalytic system over *g*-MoS<sub>2</sub>/PGBC and participate in the degradation of TC and its oxidized intermediates.

Surface properties, such as large specific surface area, excellent pore structure and unsaturated edge bonds endow the *g*-MoS<sub>2</sub>/PGBC with considerably strong adsorption capacity through mechanisms of electrostatic attraction, π-π stacking, hydrogen bonding, and pore-filling, which can attract and accumulate pollutants towards the catalyst surface. Owing to the optimized energy band gaps, *g*-MoS<sub>2</sub> could be excited and generated electron-hole pairs under visible light irradiation. The standard redox potential of O<sub>2</sub>/·O<sub>2</sub><sup>−</sup> (−0.33 eV) is negative than

conduction band (CB) potential of *g*-MoS<sub>2</sub> according to the previous reports [31,53], yet the CB potential of *g*-MoS<sub>2</sub>/PGBC is more negative than E<sub>0</sub> (O<sub>2</sub>/H<sub>2</sub>O<sub>2</sub>) (0.695 eV), which suggests that oxygen molecules attached onto the surface do not directly become superoxide radicals but could be reduced to hydrogen peroxide which is further broken down into hydroxyl radicals. Similarly, the absolute value of valence band potential of *g*-MoS<sub>2</sub>/PGBC is less than that of E (·OH/OH<sup>−</sup>) (+2.38 eV), it reveals that generated-h<sup>+</sup> directly oxidize and decompose TC molecules, instead of reacting with water molecules to form ·OH. The incorporation of PGBC with ultrathin structure, porosity and graphitization contributes to shorter charge transfer path and displays good conductivity. Intimate contact between *g*-MoS<sub>2</sub> and PGBC can accelerate the fluent transfer of free carriers on interface with PGBC acting as electron or hole-mediator for limiting charge carrier recombination. However, ESR experiments proved that ·O<sub>2</sub><sup>−</sup> do exist in photocatalytic systems, which may be explained by the phenomenon that photo-generated electrons would transfer smoothly from *g*-MoS<sub>2</sub> to PGBC through the Mo-O-C bonds and then react with the oxygen that adsorbed on the PGBC surface. Oxygen-containing functional groups favor the formation of persistent free radical (PFRs) in carbon-based materials with transition metal [54]. A small amount of oxidation Mo<sup>6+</sup> in *g*-MoS<sub>2</sub>/PGBC acts as an electron acceptor to further promote PFRs production. On the basis of these analyses, besides the schematic illustration shown in Fig. 8, the specific photocatalytic degradation process of TC by *g*-MoS<sub>2</sub>/PGBC can be described as following equations:



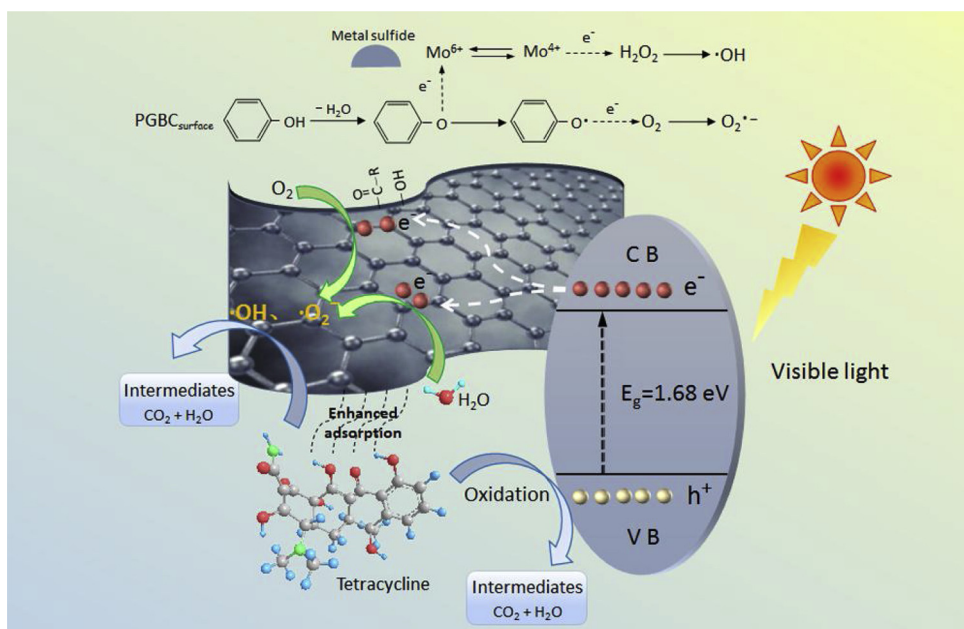
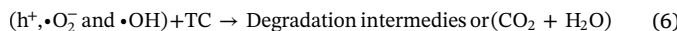
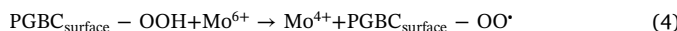


**Fig. 8.** Schematic illustration of the proposed mechanism for the degradation behavior of TC molecules by g-MoS<sub>2</sub>/PGBC nanocomposite under visible light irradiation.



#### 4. Conclusion

In conclusion, a novel nanocomposite of porous graphite biochar decorated with g-MoS<sub>2</sub> nanosheets has been rationally designed and synthesized via a facile one-pot hydrothermal method as photocatalyst for TC removal. This easily synthesized g-MoS<sub>2</sub>/PGBC exhibits considerable TC removal efficiency in various solution medium through combined functions of adsorption and photocatalysis. The porous graphite biochar as supporting is regarded as charge transporter with good conductivity, which promotes the fluent transfer of photo-generated charge carriers and hinders the recombination of electron-hole pairs. Excellent photocatalytic performance should be derived from the synergistic effects of g-MoS<sub>2</sub> and PGBC, resulting from more desirable active sites and higher photo-generated charge utilization for photocatalysis. The adsorption mechanisms, including electrostatic interaction, π-π stacking, hydrogen bonding, and pore-filling, are involved in the attraction and collection of TC molecules onto the material surface. Moreover, the h<sup>+</sup> and ·OH produced on the photocatalyst surface under visible light irradiation are predominant active species for the decomposition of adsorbed TC. Considering the efficient and stable photo-degradation of TC, g-MoS<sub>2</sub>/PGBC is regarded as a potential and sustainable photocatalyst for wide application in antibiotics-polluted natural water remediation.

#### Acknowledgments

This research was financially supported by the National Natural Science Foundation of China (81773333, 51521006, 51479072, 51809011, 51378190, 51679082 and 51809089) and the Program for Changjiang Scholars and Innovative Research Team in University (IRT-13R17).

#### Appendix A. Supplementary data

Supplementary material related to this article can be found, in the online version, at doi:<https://doi.org/10.1016/j.apcatb.2019.03.004>.

#### References

- [1] Z. Huang, K. He, Z. Song, G. Zeng, A. Chen, L. Yuan, H. Li, L. Hu, Z. Guo, Z.G. Chen, Chemosphere 211 (2018) 573–583.
- [2] X.Y. Ren, G.M. Zeng, L. Tang, J.J. Wang, J. Wan, Y.N. Liu, J.F. Yu, H. Yi, S.J. Ye, R. Deng, Sci. Total Environ. 610 (2019) 1154–1163.
- [3] S. Ye, G. Zeng, H. Wu, C. Zhang, J. Dai, J. Liang, J. Yu, X. Ren, H. Yi, M. Cheng, C. Zhang, Crit. Rev. Biotechnol. 37 (2017) 1062–1076.
- [4] L.H. Zhang, J.C. Zhang, G.M. Zeng, H.R. Dong, Y.N. Chen, C. Huang, Y. Zhu, R. Xu, Y.J. Cheng, K.J. Hou, W.C. Cao, W. Fang, Bioresour. Technol. 261 (2018) 10–18.
- [5] X. Tang, G. Zeng, C. Fan, M. Zhou, L. Tang, J. Zhu, J. Wan, D. Huang, M. Chen, P. Xu, C. Zhang, Lu Y, W. Xiong, Sci. Total Environ. 636 (2018) 1355–1361.
- [6] H.P. Wu, C. Lai, G.M. Zeng, J. Liang, J. Chen, J.J. Xu, J. Dai, X.D. Li, J.F. Liu, M. Chen, L.H. Lu, L. Hu, J. Wan, Crit. Rev. Biotechnol. 37 (2017) 754–764.
- [7] S.J. Ye, G.M. Zeng, H.P. Wu, C. Zhang, J. Liang, J. Dai, Z.F. Liu, W.P. Xiong, J. Wan, P. Xu, M. Cheng, Crit. Rev. Environ. Sci. Technol. 47 (2017) 1528–1553.
- [8] K. He, G.Q. Chen, G.M. Zeng, A.W. Chen, Z.Z. Huang, J.B. Shi, T.T. Huang, M. Peng, L. Hu, Appl. Catal. B: Environ. 228 (2018) 19–28.
- [9] Y. Yang, Z.T. Zeng, C. Zhang, D.L. Huang, G.M. Zeng, R. Xiao, C. Lai, C.Y. Zhou, H. Guo, W.J. Xue, M. Cheng, W.J. Wang, J.J. Wang, Chem. Eng. J. 349 (2018) 808–821.
- [10] C.Y. Zhou, C. Lai, D.L. Huang, G.M. Zeng, C. Zhang, M. Cheng, L. Hu, J. Wan, W.P. Xiong, M. Wen, X.F. Wen, L. Qin, Appl. Catal. B: Environ. 220 (2018) 202–210.
- [11] Y.R. Wang, Y. Zhu, Y. Hu, G.M. Zeng, Y. Zhang, C. Zhang, C.L. Feng, Small 14 (2018) 17.
- [12] W.P. Xiong, Z.T. Zeng, X. Li, G.M. Zeng, R. Xiao, Z.H. Yang, Y.Y. Zhou, C. Zhang, M. Cheng, L. Hu, C.Y. Zhou, L. Qin, R. Xu, Y.R. Zhang, Chemosphere 210 (2018) 1061–1069.
- [13] P. Xu, G.M. Zeng, D.L. Huang, C.L. Feng, S. Hu, M.H. Zhao, C. Lai, Z. Wei, C. Huang, G.X. Xie, Z.F. Liu, Sci. Total Environ. 424 (2012) 1–10.
- [14] Y.N. Gong, D.L. Li, C.Z. Luo, Q. Fu, C.X. Pan, Green Chem. 19 (2017) 4132–4140.
- [15] W.L. Gu, L.Y. Hu, J. Li, E.K. Wang, J. Mater. Chem. A 4 (2016) 14364–14370.
- [16] S.B. Yoon, G.S. Choi, S.K. Kang, J.S. Yu, K.P. Gierszal, M. Jaromiec, J. Am. Chem. Soc. 127 (2005) 4188–4189.
- [17] J.L. Gong, B. Wang, G.M. Zeng, C.P. Yang, C.G. Niu, Q.Y. Niu, W.J. Zhou, Y. Liang, J. Hazard. Mater. 164 (2009) 1517–1522.
- [18] X. Tan, Y. Liu, G. Zeng, X. Wang, X. Hu, Y. Gu, Z. Yang, Chemosphere 125 (2015) 70–85.
- [19] S.J. Ye, G.M. Zeng, H.P. Wu, J. Liang, C. Zhang, J. Dai, W.P. Xiong, B. Song, S.H. Wu, J.F. Yu, Resour. Conserv. Recycl. 140 (2019) 278–285.
- [20] L. Chen, Z.Y. Wang, He C.N, N.Q. Zhao, C.S. Shi, E.Z. Liu, J.J. Li, ACS Appl. Mater. Interfaces 5 (2013) 9537–9545.
- [21] L.X. Zuo, W.J. Wang, R.B. Song, J.J. Lv, L.P. Jiang, J.J. Zhu, ACS Sustain. Chem. Eng. 5 (2017) 10275–10282.

[22] L.J. Xie, G.H. Sun, F.Y. Su, X.Q. Guo, Q.Q. Kong, Li X.M., X.H. Huang, L. Wan, W. Song, K.X. Li, C.X. Lv, C.M. Chen, J. Mater. Chem. A 4 (2016) 1637–1646.

[23] X.H. Liu, Y. Liu, S.Y. Lu, W. Guo, B.D. Xi, Chem. Eng. J. 350 (2018) 131–147.

[24] K.K. Paul, N. Sreekanth, R.K. Biroju, T.N. Narayanan, P.K. Giri, Sol. Energy Mater. Sol. Cells 185 (2018) 364–374.

[25] L. Qin, G.M. Zeng, C. Lai, D.L. Huang, P. Xu, C. Zhang, M. Cheng, X.G. Liu, S.Y. Liu, B.S. Li, Y. Yi, Coordin. Chem. Rev. 359 (2018) 1–31.

[26] Y. Yang, C. Zhang, C. Lai, G. Zeng, D. Huang, M. Cheng, J. Wang, F. Chen, C. Zhou, W. Xiong, Adv. Colloid Interface Sci. 254 (2018) 76–93.

[27] H. Yi, D.L. Huang, L. Qin, G.M. Zeng, C. Lai, M. Cheng, S.J. Ye, B. Song, X.Y. Ren, X.Y. Guo, Appl. Catal. B: Environ. 239 (2018) 408–424.

[28] J. Theerthagiri, R.A. Senthil, B. Senthilkumar, A. Reddy Polu, J. Madhavan, M. Ashokkuma, J. Solid State Chem. 252 (2017) 43–71.

[29] D. Wang, Y. Xu, F. Sun, Q.H. Zhang, P. Wang, X.Y. Wang, Appl. Surf. Sci. 377 (2016) 221–227.

[30] S.V.P. Vattikuti, C. Byon, Superlattice. Microst. 100 (2016) 514–525.

[31] M.H. Wu, L. Li, Y.C. Xue, G. Xu, L. Tang, N. Liu, W.Y. Huang, Appl. Catal. B: Environ. 228 (2018) 103–112.

[32] Z.Z. Zhang, L. Huang, J.J. Zhang, F.J. Wang, Y.Y. Xie, X.T. Shang, Y.Y. Gu, H.B. Zhao, X.X. Wang, Appl. Catal. B: Environ. 233 (2018) 112–119.

[33] L. Yuwen, F. Xu, B. Xue, Z. Luo, Q. Zhang, B. Bao, S. Su, L. Weng, W. Huang, L. Wang, Nanoscale 6 (2014) 5762–5769.

[34] C.S. Zhu, L. Zhang, B. Jiang, J.T. Zheng, P. Hu, S.J. Li, M.B. Wu, W.T. Wu, Appl. Surf. Sci. 377 (2016) 99–108.

[35] F. Chen, Q. Yang, X.M. Li, G.M. Zeng, D.B. Wang, Niu C.G, J.W. Zhao, H.X. An, T. Xie, Y.C. Deng, Appl. Catal. B: Environ. 200 (2017) 330–342.

[36] C.Y. Zhou, C. Lai, C. Zhang, G.M. Zeng, D.L. Huang, M. Cheng, L. Hu, W.P. Xiong, M. Chen, J.J. Wang, Y. Yang, L.B. Jiang, Appl. Catal. B: Environ. 238 (2018) 6–18.

[37] Z. Zeng, S. Ye, H. Wu, R. Xiao, G. Zeng, J. Liang, C. Zhang, J. Yu, Y. Fang, B. Song, Sci. Total Environ. 648 (2018) 206–217.

[38] K. Chang, W.X. Chen, ACS Nano (2011) 4720–4728.

[39] Y.J. Zhao, X.W. Zhang, C.Z. Wang, Y.Z. Zhao, H.P. Zhou, J.B. Li, H.B. Jin, Appl. Surf. Sci. 412 (2017) 207–213.

[40] X.H. Zhang, K. Zhang, H.X. Li, Q. Wang, L.E. Jin, Q. Cao, J. Appl. Electrochem. 48 (2018) 415–426.

[41] L. Yang, X. Zheng, M. Liu, S. Luo, Y. Luo, G. Li, J. Hazard. Mater. 329 (2017) 230–240.

[42] Y.H. Chao, W.S. Zhu, X.Y. Wu, F.F. Hou, S.H. Xun, P.W. Wu, H.Y. Ji, H. Xu, H.M. Li, Chem. Eng. J. 243 (2014) 60–67.

[43] L. Wang, G. Mu, C. Tian, L. Sun, W. Zhou, P. Yu, J. Yin, H. Fu, ChemSusChem 6 (2013) 880–889.

[44] S. Han, K. Liu, L. Hu, F. Teng, P. Yu, Y. Zhu, Sci. Rep.-UK 7 (2017) 43599.

[45] J.C. Yan, L. Han, W.G. Gao, S. Xue, M.F. Chen, Bioresour. Technol. 175 (2015) 269–274.

[46] X.Q. Qiao, F.C. Hu, F.Y. Tian, D.F. Hou, D.S. Li, RSC Adv. 6 (2016) 11631–11636.

[47] L. Xu, L. Yang, E.M.J. Johansson, Y.H. Wang, P.K. Jin, Chem. Eng. J. 350 (2018) 1043–1055.

[48] E. Erdogan, I.H. Popov, A.N. Enyashin, G. Seifert, Eur. Phys. J. B 85 (2012) (2012) 392.

[49] C. Feng, Z.Y. Chen, J. Hou, J.R. Li, X.B. Li, L.K. Xu, M.X. Sun, R.C. Zeng, Chem. Eng. J. 345 (2018) 404–413.

[50] J. Xu, L. Wang, Y. Zhu, Langmuir 28 (2012) 8418–8425.

[51] Y.H. Chao, L. Yang, H.Y. Ji, W.S. Zhu, J.Y. Pang, C.R. Han, H.M. Li, Environ. Prog. Sustain. 36 (2017) 815–821.

[52] A. Abdelhaleem, W. Chu, J. Hazard. Mater. 338 (2017) 491–501.

[53] W.C. Peng, Y. Chen, X.Y. Li, J. Hazard. Mater. 309 (2016) 173–179.

[54] G. Fang, C. Liu, J. Gao, D.D. Dionysiou, D. Zhou, Environ. Sci. Technol. 49 (2015) 5645–5653.